Available online at https://link.springer.com/journal/42241
http://www.jhydrodynamics.com
Journal of Hydrodynamics, 2019, 31(4): 827-839
https://doi.org/10.1007/s42241-018-0171-x

A compact streamfunction-velocity scheme for the 2-D unsteady incompressible Navier-Stokes equations in arbitrary curvilinear coordinates *

Jian-xin Qiu, Bo Peng, Zhen-fu Tian
Department of Mechanics and Engineering Science, Fudan University, Shanghai 200433, China

(Received July 10, 2017, Revised December 16, 2017, Accepted December 27, 2017, Published online December 29, 2018)
©China Ship Scientific Research Center 2019

Abstract: A streamfunction-velocity formulation-based compact difference method is suggested for solving the unsteady incompressible Navier-Stokes equations in the arbitrary curvilinear coordinates, in which the streamfunction and its first derivatives as the unknown variables are utilized. Numerical examples, involving the boundary layer problem, a constricted channel flow, driven polar cavity flow and trapezoidal cavity flow problem, are solved by the present method. Numerical results demonstrate the accuracy of the proposed scheme and exhibit the numerical capability to simulate the flow problems on geometries beyond rectangular. For driven polar cavity flow problem, the results show that the flow for $Re = 5\,000$ is not steady but time-periodic, and the critical Reynold number (Re_c) for the occurrence of a Hopf bifurcation is given.

Key words: Streamfunction-velocity formulation, arbitrary curvilinear coordinates, compact scheme, unsteady, incompressible flow

Introduction

Over the past few years, as a significant alternative computational technique to 2-D Navier-Stokes (N-S) equations solvers, the streamfunction-velocity or pure streamfunction approach has captured more attentions. The vorticity formulation (vorticity-velocity and streamfunction-vorticity)[1-5], due to the absence of the physical boundary conditions for the vorticity, the corresponding numerical approximation for the vorticity boundary has to be supplemented. By comparison with vorticity formulation, the boundary conditions of velocity and streamfunction in the streamfunction-velocity or pure streamfunction formulation are generally known and are not difficult to implement computationally. However, the governing equation based on the streamfunction-velocity formulation is a fourth order nonlinear partial differential equation, such that a uniform grid with 13 grid points is carried out to acquire a classical second-order finite difference (FD) scheme when the streamfunction-velocity formulation is approached via the FD method. Whence the FD scheme using 13 points has to be amended at grid points in the vicinity of the boundaries and there are further difficulties with the solution of the resulting linear systems. To eliminate these pitfalls, a variety of compact schemes with respect to the streamfunction-velocity formulation have been proposed and are very efficient and accurate[6-12]. These compact schemes are confined invariably to only rectangular regions, so that they could not fully exploit the advantages associated with non-rectangular geometric problem, that of smaller scales in the regions of large gradients in particular. As a matter of fact, many flow problems, such as large gradient boundary layer problems, have uneven distribution in various places. Hence, it is extremely indispensable to establish effective numerical algorithms for simulating the flow in geometries beyond rectangular. Fortunately, some relevant researches have begun to be performed for the streamfunction-velocity or pure streamfunction formulation of the incompressible N-S equations based on the irregular planar domains. Yu and Tian[13] addressed a compact streamfunction-velocity scheme for a steady 2-D incompressible N-S equations via the polar coordinates transformation based on five-point stencil. Pandit[14] developed a new methodology based on

* Project supported by the National Natural Science Foundation of China (Grant Nos. 11872151, 11372075, 91330112 and 11502054).
Biography: Jian-xin Qiu (1987-), Male, Ph. D.,
E-mail: edisonyan@live.cn
Corresponding author: Zhen-fu Tian,
E-mail: zftian@fudan.edu.cn

streamfunction velocity formulation for a steady biharmonic equation on irregular geometries, and the gradient of streamfunction (or velocity) is replaced through the second-order central difference scheme. Shortly afterwards, Sen et al.[15] presented an implicit compact scheme for 2-D unsteady flows in which the fourth-order pure streamfunction equation is transformed by a conformal mapping. These methods mentioned above[13-15] have the following several characters. On the one hand, the methods in Refs. [14-15] have been developed based on a conformal transformation rather than the arbitrary coordinate transformation, so that it may be invalid for the non-conformal transformation cases. The compact schemes in Refs. [13-14] merely happen to be applied to steady problems. On the other hand, these discrete difference schemes are based on the nine-point compact stencil except for the literature[13]. As mentioned in Ref. [7], they are called as nine-point variable coefficient second-order compact scheme, i.e., the influences coefficients of the finite difference formulation for the streamfunction are connected to Reynolds number, grid size and streamfunction gradient, thus making the discrete algebra systems have stronger nonlinearity. For five-point compact scheme, the coefficient matrix is constant and gives rise to a strictly dominant block tri-diagonal system of equations. In the present paper, we extend this five-point compact scheme to the arbitrary curvilinear coordinates. In addition, the element involving the discrete coefficient matrix contains the unknown streamfunction gradient so that it is variable coefficient matrix in each iteration step. Meanwhile, the coefficient matrix is not completely diagonally dominant matrix and may become ill-conditioned matrix during the iterations. As a result, one can hardly obtain convergence results using traditional iterative method.

In the present study, we establish a new five-point constant coefficient compact stream-function-velocity scheme for the 2-D unsteady N-S equations based on the arbitrary curvilinear coordinates. The coefficient matrix is constant and strictly penta-diagonal dominant which can ensure stability for the algebraic system utilizing conventional iterative method and also decrease significantly the computational complexity. To check the proposed scheme, we are concerned with an analytical solution for the boundary layer, a constricted channel problem, driven polar cavity flow and trapezoidal cavity flow problem.

1. The mathematical formulation and numerical method

1.1 *The mathematical formulation*

Considering the streamfunction-vorticity $(\psi-\zeta)$ formulation of the unsteady incompressible N-S equations in the Cartesian coordinates (x,y) is

$$-\psi_{xx}-\psi_{yy}=\zeta \tag{1}$$

$$\frac{\partial\zeta}{\partial t}-\frac{1}{Re}(\zeta_{xx}+\zeta_{yy})+u\frac{\partial\zeta}{\partial x}+\frac{\partial\zeta}{\partial y}=S \tag{2}$$

where u, v are the velocities, ψ, ζ are the streamfunction, vorticity respectively, S is the source term, and Re is the Reynolds number. For the sake of convenience, Eqs. (1), (2) can be expressed as the unified formulation

$$\widetilde{a}_i\frac{\partial^2\Phi_i}{\partial x^2}+\widetilde{g}_i\frac{\partial^2\Phi_i}{\partial x\partial y}+\widetilde{b}_i\frac{\partial^2\Phi_i}{\partial y^2}+\widetilde{c}_i\frac{\partial\Phi_i}{\partial x}+\widetilde{d}_i\frac{\partial\Phi_i}{\partial y}+\widetilde{e}_i\Phi_i=$$

$$\widetilde{F}_i(x,y),\ \ i=1,2 \tag{3}$$

where Φ_1, Φ_2 stand for streamfunction ψ and vorticity ζ. The coefficients and the source terms are given by

$$\widetilde{a}_1=\widetilde{b}_1=-1,\ \ \widetilde{g}_1=0,\ \ \widetilde{c}_1=\widetilde{d}_1=\widetilde{e}_1=0,\ \ \widetilde{F}_1=\zeta,$$

$$\widetilde{a}_2=\widetilde{b}_2=-1,\ \ \widetilde{g}_2=0,\ \ \widetilde{c}_2=uRe,\ \ \widetilde{d}_2=vRe,\ \ \widetilde{e}_2=0,$$

$$\widetilde{F}_2=ReS-Re\frac{\partial\zeta}{\partial t} \tag{4}$$

Now, we use the coordinate transformation to extend this formulation to a general coordinate system (ξ,η). The relationship of the coordinate transformation is following:

$$x=x(\xi,\eta),\ \ y=y(\xi,\eta) \tag{5}$$

Under this transformation, the above Eq. (3) is transformed as

$$a_i\frac{\partial^2\Phi_i}{\partial\xi^2}+g_i\frac{\partial^2\Phi_i}{\partial\xi\partial\eta}+b_i\frac{\partial^2\Phi_i}{\partial\eta^2}+c_i\frac{\partial\Phi_i}{\partial\xi}+d_i\frac{\partial\Phi_i}{\partial\eta}+$$

$$e_i\Phi_i=F_i(\xi,\eta),\ \ i=1,2 \tag{6}$$

The coefficients are given by

$$a_i(\xi,\eta)=\frac{1}{J^2}(\hat{b}_i x_\eta^2+\hat{a}_i y_\eta^2),$$

$$b_i(\xi,\eta)=\frac{1}{J^2}(\hat{b}_i x_\xi^2+\hat{a}_i y_\xi^2),$$

$$c_i(\xi,\eta)=\frac{1}{J}[\hat{c}_i y_\eta-\hat{d}_i x_\eta+R_{1i}(\xi,\eta),$$

$$d_i(\xi,\eta)=\frac{1}{J}[\hat{d}_i x_\xi-\hat{c}_i y_\xi+R_{2i}(\xi,\eta)],$$

$$g_i(\xi,\eta)=-\frac{2}{J^2}(\hat{a}_i y_\xi y_\eta+\hat{b}_i x_\xi x_\eta),\quad e_i(\xi,\eta)=\hat{e}_i,$$

$$F_1(\xi,\eta)=\zeta,\quad F_2(\xi,\eta)=ReS-Re\frac{\partial\zeta}{\partial t} \tag{7}$$

and

$$R_{1i}(\xi,\eta)=a_i(\xi,\eta)(y_{\xi\xi}x_\eta-x_{\xi\xi}y_\eta)+$$
$$g_i(\xi,\eta)(y_{\xi\eta}x_\eta-x_{\xi\eta}y_\eta)+b_i(\xi,\eta)(y_{\eta\eta}x_\eta-x_{\xi\xi}y_\eta),$$
$$R_{2i}(\xi,\eta)=a_i(\xi,\eta)(x_{\xi\xi}y_\xi-y_{\xi\xi}x_\xi)+$$
$$g_i(\xi,\eta)(x_{\xi\eta}y_\xi-y_{\xi\eta}x_\xi)+b_i(\xi,\eta)(x_{\eta\eta}y_\xi-y_{\eta\eta}x_\xi) \tag{8}$$

where $\hat{a}_i,\hat{b}_i,\hat{g}_i,\hat{c}_i,\hat{d}_i,\hat{e}_i$ are the transformed forms in (ξ,η) (ξ,η) plane of the coefficients $\hat{a}_i,\hat{b}_i,\hat{g}_i,\hat{c}_i,\hat{d}_i,\hat{e}_i$ in (x,y) plane, respectively. $J=x_\xi y_\eta-x_\eta y_\xi$ is the Jacobian of the transformation.

And then, eliminating vorticity ζ, the stream-function-velocity formulation of N-S equation in the general curvilinear coordinate system is obtained by

$$A\frac{\partial^4\psi}{\partial\xi^4}+B\frac{\partial^4\psi}{\partial\xi^3\partial\eta}+C\frac{\partial^4\psi}{\partial\xi^2\partial\eta^2}+D\frac{\partial^4\psi}{\partial\xi\partial\eta^3}+$$
$$E\frac{\partial^4\psi}{\partial\eta^4}+F\frac{\partial^3\psi}{\partial\xi^3}+G\frac{\partial^3\psi}{\partial\xi^2\partial\eta}+H\frac{\partial^3\psi}{\partial\xi\partial\eta^2}+$$
$$K\frac{\partial^3\psi}{\partial\eta^3}+L\frac{\partial^2\psi}{\partial\xi^2}+M\frac{\partial^2\psi}{\partial\xi\partial\eta}+N\frac{\partial^2\psi}{\partial\eta^2}+$$
$$P\frac{\partial\psi}{\partial\xi}+Q\frac{\partial\psi}{\partial\eta}+R\psi(\xi,\eta)=F_2(\xi,\eta) \tag{9}$$

where the coefficients $A,B,C,D,E,F,G,H,K,L,M,N,P,Q,R$ given explicitly as follows:

$A=a_1a_2$, $B=a_2g_1+a_1g_2$, $C=a_2b_1+g_1g_2+a_1b_2$,

$D=b_2g_1+g_1b_2$, $E=b_1b_2$,

$F=2a_2a_{1\xi}+g_2a_{1\eta}+a_2c_1+a_1c_2$,

$G=2b_2a_{1\eta}+2a_2g_{1\xi}+g_2a_{1\xi}+g_2g_{1\eta}+a_2d_1+$
$d_2a_1+c_2g_1+c_1g_2$,

$H=2a_2b_{1\xi}+2b_2g_{1\eta}+g_2b_{1\eta}+g_2g_{1\xi}+b_2c_1+$
$c_2b_1+d_2g_1+d_1g_2$,

$K=2b_2b_{1\eta}+g_2b_{1\xi}+b_1d_2+b_2d_1$,

$L=a_2a_{1\xi\xi}+b_2a_{1\eta\eta}+g_2a_{1\xi\eta}+2a_2c_{1\xi}+c_2a_{1\xi}+$
$d_2a_{1\eta}+g_2c_{1\eta}+c_1c_2+a_1e_2+a_2e_1$,

$M=a_2g_{1\xi\xi}+b_2g_{1\eta\eta}+g_2g_{1\xi\eta}+2a_2d_{1\xi}+2b_2c_{1\eta}+$
$c_2g_{1\xi}+g_2c_{1\xi}+d_2g_{1\eta}+g_2d_{1\eta}+$
$c_1d_2+c_2d_1+g_1e_2+g_2e_1$,

$N=a_2b_{1\xi\xi}+b_2b_{1\eta\eta}+g_2b_{1\xi\eta}+2b_2d_{1\eta}+c_2b_{1\xi}+$
$d_2b_{1\eta}+g_2d_{1\xi}+d_1d_2+b_1e_2+b_2e_1$,

$P=a_2c_{1\xi\xi}+b_2c_{1\eta\eta}+g_2c_{1\xi\eta}+2a_2e_{1\xi}+c_2c_{1\xi}+$
$d_2c_{1\eta}+g_2e_{1\eta}+c_1e_2+c_2e_1$,

$Q=a_2d_{1\xi\xi}+b_2d_{1\eta\eta}+g_2d_{1\xi\eta}+2b_2e_{1\eta}+c_2d_{1\xi}+$
$d_2d_{1\eta}+g_2e_{1\xi}+d_1e_2+d_2e_1$,

$R=a_2e_{1\xi\xi}+b_2e_{1\eta\eta}+g_2e_{1\xi\eta}+c_2e_{1\xi}+d_2e_{1\eta}+e_1e_2$

In addition, the relations between the velocities (u, v) and the first derivations of the streamfunction (ψ_ξ, ψ_η) are given by

$$u=\frac{1}{J}(\psi_\eta x_\xi-\psi_\xi x_\eta),\quad v=\frac{1}{J}(\psi_\eta y_\xi-\psi_\xi y_\eta) \tag{10}$$

$$\psi_\xi = -vx_\xi + uy_\xi,\ \psi_\eta = -vx_\eta + uy_\eta \tag{11}$$

From Eq. (11), we can easily obtain the boundary conditions for the first derivations of the stream-function. Using Eq. (10), we can determine the values of the velocities by ψ_ξ, ψ_η to update those coefficients in Eq. (9).

1.2 *The discretization scheme*

For convenience, standard central difference operators with first and second derivatives at each internal nodal point (ξ_i, η_j) are given by

$$\delta_\xi \phi = \frac{\phi_1 - \phi_3}{2h_\xi},\ \delta_\xi^2 \phi = \frac{\phi_1 - 2\phi_0 + \phi_3}{h_\xi^2},\ \delta_\eta \phi = \frac{\phi_2 - \phi_4}{2h_\eta},$$

$$\delta_\eta^2 \phi = \frac{\phi_2 - 2\phi_0 + \phi_4}{h_\eta^2} \tag{12}$$

where h_ξ, h_η denote the spatial increment in x-, y-directions, 0, 1, 2, 3, 4, 5, 6, 7, 8 stand for grid points $(\xi_i, \eta_j), (\xi_{i+1}, \eta_j), (\xi_i, \eta_{j+1}), (\xi_{i-1}, \eta_j), (\xi_i, \eta_{j-1})$, $(\xi_{i+1}, \eta_{j+1}), (\xi_{i-1}, \eta_{j+1}), (\xi_{i-1}, \eta_{j-1}), (\xi_{i+1}, \eta_{j-1})$, respectively.

In Eq. (9), all derivative terms of the stream-function ψ are replaced by the first and second derivative of the streamfunction gradients ψ_ξ, ψ_η except for the fourth derivative terms $\partial^4\psi/\partial\xi^4$ and $\partial^4\psi/\partial\eta^4$. And the newly governing Eq. (9) is discretized by using the standard central difference operators as follows

$$\left\{ A\delta_\xi^4 \psi + B\delta_\xi^2 \delta_\eta \psi_\xi + \right.$$

$$\frac{C}{2}(\delta_\xi^2 \delta_\eta \psi_\eta + \delta_\xi \delta_\eta^2 \psi_\xi) + D\delta_\xi \delta_\eta^2 \psi_\eta +$$

$$E\delta_\eta^4 \psi + F\delta_\xi^2 \psi_\xi + G\delta_\xi^2 \psi_\eta + H\delta_\eta^2 \psi_\xi +$$

$$K\delta_\eta^2 \psi_\eta + L\delta_\xi \psi_\xi + \frac{M}{2}(\delta_\xi \psi_\eta + \delta_\eta \psi_\xi) +$$

$$\left. N\delta_\eta \psi_\eta + P\psi_\xi + Q\psi_\eta + R\psi \right\}_{i,j} =$$

$$F_{2i,j} + O(h_\xi^2 + h_\xi h_\eta + h_\eta^2) \tag{13}$$

where the following Stephenson finite difference operators are employed to approximate the difference operators $\delta_\xi^4 \psi$, $\delta_\eta^4 \psi$

$$\delta_\xi^4 \psi = \frac{12}{h_\xi^2}(\delta_\xi \psi_\xi - \delta_\xi^2 \psi),\ \delta_\eta^4 \psi = \frac{12}{h_\eta^2}(\delta_\eta \psi_\eta - \delta_\eta^2 \psi) \tag{14}$$

And the following Padé schemes are chosen to approach the stream function gradients ψ_ξ, ψ_η

$$\psi_\xi = \left(\delta_\xi \psi - \frac{h_\xi^2}{6}\delta_\xi^2 \psi_\xi \right) + O(h_\xi^4),$$

$$\psi_\eta = \left(\delta_\eta \psi - \frac{h_\eta^2}{6}\delta_\eta^2 \psi_\eta \right) + O(h_\eta^4) \tag{15}$$

Meanwhile, using second-order Crank-Nicolson scheme with a temporal increment Δt for approaching the time derivative, and the discrete scheme of Ref. [9] can be written by

$$\sum_{k=0}^{4} A_k \psi_k^{n+1} = \sum_{k=0}^{4} B_k \psi_k^n - \frac{1}{2}(f^n + f^{n+1}) \tag{16}$$

The coefficients of Eq. (16) are listed as follows:

$$A_0 = \frac{1}{\Delta t}\left(e_1 - \frac{2a_1}{h_\xi^2} - \frac{2b_1}{h_\eta^2} \right) + \left(\frac{12A}{h_\xi^4} + \frac{12E}{h_\eta^4} + \frac{R}{2} \right),$$

$$A_1 = A_3 = \frac{1}{\Delta t}\frac{a_1}{h_\xi^2} - \frac{6A}{h_\xi^4},\ A_2 = A_4 = \frac{1}{\Delta t}\frac{b1}{h_\eta^2} - \frac{6E}{h_\eta^4},$$

$$B_0 = \frac{1}{\Delta t}\left(e_1 - \frac{2a_1}{h_\xi^2} - \frac{2b_1}{h_\eta^2} \right) - \left(\frac{12A}{h_\xi^4} + \frac{12E}{h_\eta^4} - \frac{R}{2} \right),$$

$$B_1 = B_3 = \frac{1}{\Delta t}\frac{a_1}{h_\xi^2} + \frac{6A}{h_\xi^4},\ B_2 = B_4 = \frac{1}{\Delta t}\frac{b_1}{h_\eta^2} + \frac{6E}{h_\eta^4} \tag{17}$$

and

$$f^n = \frac{12A}{h_\xi^2}\delta_\xi \psi_\xi^n + \frac{12E}{h_\eta^2}\delta_\eta \psi_\eta^n +$$

$$\frac{g_1}{2}(\delta_t^+ \delta_\xi \psi_\eta^{n-1} + \delta_t^+ \delta_\eta \psi_\xi^{n-1}) + c_1 \delta_t^+ \psi_\xi^{n-1} +$$

$$d_1 \delta_t^+ \psi_\eta^{n-1} + B\delta_\xi^2 \delta_\eta \psi_\xi^n + \frac{C}{2}(\delta_\xi^2 \delta_\eta \psi_\eta^n + \delta_\xi \delta_\eta^2 \psi_\xi^n) +$$

$$D\delta_\xi\delta_\eta^2\psi_\eta^n + F\delta_\xi^2\psi_\xi^n + G\delta_\xi^2\psi_\eta^n + H\delta_\eta^2\psi_\xi^n +$$

$$K\delta_\eta^2\psi_\eta^n + L\delta_\xi\psi_\xi^n + \frac{M}{2}(\delta_\eta\psi_\xi^n + \delta_\xi\psi_\eta^n) + N\delta_\eta\psi_\eta^n +$$

$$P\psi_\xi^n + Q\psi_\eta^n - F_2^n$$

where $\delta_t^+\phi_{ij}^n = (\phi_{ij}^{n+1} - \phi_{ij}^n)/\Delta t$ is the forward difference operator.

1.3 *The algebraic system*

Next, we discuss the solution of algebraic system associated with the newly proposed algorithm, and the matrix form of the system can be written as follows

$$A\boldsymbol{\Psi}^{n+1} = \boldsymbol{F}(\boldsymbol{\Psi}^n, \boldsymbol{\Psi}_\xi^n, \boldsymbol{\Psi}_\eta^n, \boldsymbol{\Psi}_\xi^{n+1}, \boldsymbol{\Psi}_\eta^{n+1}) \tag{18}$$

where $\boldsymbol{\Psi}^n, \boldsymbol{\Psi}_\xi^n, \boldsymbol{\Psi}_\eta^n, \boldsymbol{\Psi}^{n+1}, \boldsymbol{\Psi}_\xi^{n+1}, \boldsymbol{\Psi}_\eta^{n+1}$ and $\boldsymbol{F}$ are all the $M_1 \times M_2$ dimensional vectors. The matrix A is strictly penta-diagonal dominant matrix in the dimension $M_1 \times M_2$ for a mesh of size $M_1 \times M_2$. Furthermore, it is not arduous to find that, since a_i, b_i, e_i in Eq. (3) is constant for the given transformation of coordinates, the matrix A is also constant coefficient matrix, which can ensure stability for the discrete algebraic system in each iterative step, so that a series of algorithms like Gauss-Seidel (GS), Jacobi, successive over-relaxation (SOR) and conjugate gradient(CG) can be allowed to calculate the corresponding problem. In order to accelerate calculation, the multi-grid method is employed to solve numerically relevant problem, and specific details are referred to Refs. [3, 13]. Its entire solving procedure is briefly summarized in the following algorithm:

(1) Begin with $\psi^{n,k}$.

(2) Compute $\psi_\xi^{n,k}, \psi_\eta^{n,k}$ by Eq. (15) and take $\psi_\xi^{n+1,k+1} = \psi_\xi^{n,k}$, $\psi_\eta^{n+1,k+1} = \psi_\eta^{n,k}$.

(3) Predict $\psi^{n+1,k+1}$ using Eq. (18).

(4) Correct $\psi_\xi^{n+1,k+1}, \psi_\eta^{n+1,k+1}$ using Eq. (15).

(5) If $\left\|\psi^{n+1,k+1} - \psi^{n+1,k}\right\| \le \varepsilon_0$ where ε_0 is the convergence criterion, then $\psi^{n+1} = \psi^{n+1,k+1}$. Otherwise, set $k = k+1$ and go to step 3.

(6) March in time with $n \leftarrow n+1$ and go to step 2.

2. Stability analysis

Now we prove the stability for constant coefficients of the finite difference scheme (16) by von Neumann linear stability analysis. Taking into account the complexity of the general curvilinear coordinate system, we investigate only the stability analysis of the current scheme with a conformal transformation in here. By means of linearizing, Eq. (9) is simplified as following

$$\frac{\partial}{\partial t}\Delta\psi = a\Delta^2\psi + b\Delta\psi_\xi + c\Delta\psi_\eta + d(\delta_\xi\psi_\xi + \delta_\eta\psi_\eta) \tag{19}$$

Herein, $a > 0, b, c, d$ are assumed to be independent of ψ and its derivatives ψ_ξ, ψ_η. Ulteriorly, weighted thought is applied to Eq. (19)

$$\Delta\psi^{n+1} - \Delta t\omega[a\Delta^2\psi^{n+1} + b\Delta\psi_\xi^{n+1} + c\Delta\psi_\eta^{n+1} +$$

$$d(\delta_\xi\psi_\xi^{n+1} + \delta_\eta\psi_\eta^{n+1})] = \Delta\psi^n + \Delta t(1-\omega)\cdot$$

$$[a\Delta^2\psi^n + b\Delta\psi_\xi^n + c\Delta\psi_\eta^n + d(\delta_\xi\psi_\xi^n + \delta_\eta\psi_\eta^n)] \tag{20}$$

Theorem 1: The finite difference scheme (16) is unconditionally stable for $0.5 \le \omega \le 1$ in the von Neumann sense when $d \le 0$.

Proof: Let $\psi_{ij}^n = \Phi^n e^{I(\theta_\xi i + \theta_\eta j)}$ where Φ^n is the amplitude at time level n and $I = \sqrt{-1}$ is imaginary unit, $\theta_\xi = 2\pi h_\xi / K_1$, $\theta_\eta = 2\pi h_\eta / K_2$ are the phase angles in x-, y- directions with wavelengths K_1, K_2 respectively. Then according to Eqs. (14), (15), we have

$$\delta_\xi\psi_{ij}^{(n)} = I\frac{\sin\theta_\xi}{h_\xi}\psi_{ij}^{(n)}, \quad \delta_\eta\psi_{ij}^{(n)} = I\frac{\sin\theta_\eta}{h_\eta}\psi_{ij}^{(n)} \tag{21}$$

$$\delta_\xi^2\psi_{ij}^{(n)} = \frac{2\cos\theta_\xi - 2}{h_\xi^2}\psi_{ij}^{(n)}, \quad \delta_\eta^2\psi_{ij}^{(n)} = \frac{2\cos\theta_\eta - 2}{h_\eta^2}\psi_{ij}^{(n)} \tag{22}$$

$$\psi_{\xi ij}^{(n)} = I\frac{3\sin\theta_\xi}{h_\xi(2+\cos\theta_\xi)}\psi_{ij}^{(n)}, \quad \psi_{\eta ij}^{(n)} = I\frac{3\sin\theta_\eta}{h_\eta(2+\cos\theta_\eta)}\psi_{ij}^{(n)} \tag{23}$$

$$\psi_{\xi\xi\xi\xi\xi ij}^{(n)} = \frac{12}{h_\xi^4}\frac{(1-\cos\theta_\xi)^2}{2+\cos\theta_\xi}\psi_{ij}^{(n)},$$

$$\psi_{\eta\eta\eta\eta ij}^{(n)} = \frac{12}{h_\eta^4}\frac{(1-\cos\theta_\eta)^2}{2+\cos\theta_\eta}\psi_{ij}^{(n)} \tag{24}$$

Table 1 The L_∞ - errors and convergence rates of streamfunction for various λ, and Re

Re	Grid	Pandit[14] $\lambda=0$ Error	Rate	Pandit[14] $\lambda=0.6$ Error	Rate	Present $\lambda=0$ Error	Rate	Present $\lambda=0.3$ Error	Rate
1	21×21	3.21 (–02)	-	2.40 (–03)	-	2.32 (–03)	-	8.16 (–04)	-
	41×41	8.26 (–03)	1.96	6.39 (–04)	1.91	5.82 (–04)	2.00	2.08 (–04)	1.97
	81×81	2.10 (–03)	1.97	1.60 (–04)	1.99	1.49 (–04)	1.97	5.30 (–05)	1.97
10	21×21	2.55 (–02)	-	2.57 (–03)	-	1.80 (–03)	-	6.54 (–04)	-
	41×41	6.68 (–03)	1.93	6.51 (–04)	2.26	4.62 (–04)	1.96	1.67 (–04)	1.97
	81×81	1.60 (–03)	1.98	1.63 (–04)	2.12	1.13 (–04)	2.03	4.10 (–05)	2.03
100	21×21	1.71 (–02)	-	3.97 (–03)	-	6.99 (–04)	-	4.17 (–04)	-
	41×41	3.57 (–03)	2.26	9.66 (–04)	2.03	1.31 (–04)	2.42	1.02 (–04)	2.03
	81×81	8.23(–04)	2.12	1.88(–04)	2.36	2.65(–05)	2.31	2.64(–05)	1.94

Using relations (21)-(24) in the scheme (16), we obtain the amplification factor (G) associated with the finite difference scheme (16)

$$G=\frac{\Phi^{n+1}}{\Phi^{n}}=\frac{2A_1+A_2+IA_3}{2A_1-A_2-IA_3} \tag{25}$$

where

$$A_1=\frac{2\cos\theta_\xi-2}{h_\xi^2}+\frac{2\cos\theta_\eta-2}{h_\eta^2},$$

$$A_2=\frac{12a\Delta t}{h_\xi^4}\frac{(1-\cos\theta_\xi)^2}{2+\cos\theta_\xi}+\frac{12a\Delta t}{h_\eta^4}\frac{(1-\cos\theta_\eta)^2}{2+\cos\theta_\eta}+$$

$$\frac{6a\Delta t\sin^2\theta_\xi(1-\cos\theta_\eta)}{h_\xi^2h_\eta^2(2+\cos\theta_\xi)}+\frac{6a\Delta t\sin^2\theta_\eta(1-\cos\theta_\xi)}{h_\xi^2h_\eta^2(2+\cos\theta_\eta)}-$$

$$\frac{3d\Delta t\sin^2\theta_\xi}{h_\xi^2(2+\cos\theta_\xi)}-\frac{3d\Delta t\sin^2\theta_\eta}{h_\eta^2(2+\cos\theta_\eta)}$$

$$A_3=\frac{6b\Delta t\sin\theta_\xi(\cos\theta_\xi-1)}{h_\xi^3(2+\cos\theta_\xi)}+\frac{6b\Delta t\sin\theta_\xi(\cos\theta_\eta-1)}{h_\xi h_\eta^2(2+\cos\theta_\xi)}+$$

$$\frac{6c\Delta t\sin\theta_\eta(\cos\theta_\xi-1)}{h_\xi^2h_\eta(2+\cos\theta_\eta)}+\frac{6c\Delta t\sin\theta_\eta(\cos\theta_\eta-1)}{h_\xi h_\eta^2(2+\cos\theta_\eta)} \tag{26}$$

Hence

$$|G|^2=\frac{(2A_1+A_2)^2+A_3^2}{(2A_1-A_2)^2+A_3^2} \tag{27}$$

For stability we require $|G|^2\le 1$, and Eq. (27) is simplified as

$$A_1A_2\le 0 \tag{28}$$

Note from Eq. (26) that $A_1\le 0$, $A_2\ge 0$, thus $A_1A_2\le 0$, and the above inequality is apparently satisfied which completes the required proof.

3. Numerical results

In this section, the accuracy, effectiveness and robustness of our scheme are tested through using the analytical issues and three classical flow problems with complicated geometry. It includes the following four test problems: the boundary layer problem, a constricted channel problem, driven polar cavity flow and trapezoidal cavity flow problem.

3.1 *Boundary layer problem*

Firstly, to check the accuracy of the proposed scheme, we consider a problem governed by N-S equations with a constructed analytical solution[2], the analytical solution of this problem with respect to streamfunction is expressed by

$$\psi=\frac{(1-\mathrm{e}^{-px})(1-\mathrm{e}^{-py})}{(1-\mathrm{e}^{-p})^2},\quad (x,y)\in[0,1]\times[0,1]$$

and the source term S in Eq. (2) is given by

$$S=\frac{p^4[\mathrm{e}^{-px}+\mathrm{e}^{-py}-4\mathrm{e}^{-4(x+y)}]}{(1-\mathrm{e}^{-p})^2}$$

The boundary conditions are given by analytical solution. This problem has a steep boundary layer at $x=0$, $y=0$, and the thickness of boundary layer becomes thinner as the value of p increases. Similar to Ref. [14], we take p as 10 in our calculation. In order to capture preferably boundary layer information, the following transformation is given by

$$x(\xi,\eta)=\xi-\frac{\lambda_\xi}{\pi}\sin\pi\xi\ ,\quad y(\xi,\eta)=\eta-\frac{\lambda_\eta}{\pi}\sin\pi\eta\ ,$$

$$[\xi,\eta]\in[0,1]\times[0,1] \tag{29}$$

where λ_ξ,λ_η $(0\le\lambda_\xi,\lambda_\eta\le1)$ are the stretching parameter in x-, y-directions which determine the degree of clustering near the corresponding boundaries, respectively. The L_∞-errors and the convergence rates for streamfunction with various stretching parameter λ and Reynolds number are summarized in Table 1. Thereinto, the rate of convergence is estimated by

$$\text{Rate}=\frac{\lg(E^{2h}/E^{h})}{\lg(2)}$$

where E^{2h}, E^{h} represent the residual errors for the coarse mesh $(2h)$ and refined mesh (h) in the computational domain, respectively. And the results obtained by our proposed scheme and Pandit[14] have been compared. It is clear from Table 1 that the convergence rates of the present scheme and Pandit's scheme[14] achieve second order accuracy as expected. Furthermore, comparing the maximum absolute errors (L_∞-error), one can see that the accuracy of our proposed scheme for the uniform grid $(\lambda=0)$ with any Reynolds numbers is better than the scheme of Ref. [14], meanwhile, it also illustrates that our scheme is more accurate than the scheme of Ref. [14] not only on the uniform grid but also on the nonuniform grid.

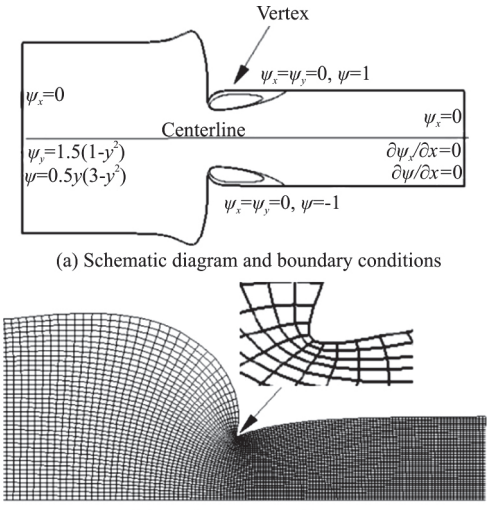

(a) Schematic diagram and boundary conditions

(b) Mesh structure with τ=0.9

Fig. 1 Schematic diagram of laboratory flume

3.2 *Constricted channel problem*

The incompressible fluid flow problem in a 2-D rigid step-down constricted channel, which has been investigated numerically in Refs. [16-18], is a basic challenge to obtain the recirculation region immediately downstream of the constriction for appropriate Reynolds numbers in numerical simulation. As shown in Fig. 1(b), with the controlling parameter τ increases, the channel boundary can be gradually varied from a smooth constriction to one with a very sharp corner, the coordinate may become singularity when the controlling parameter reaches a certain critical value. Thus τ is chosen in the range of $0<\tau\le1$ for avoiding the coordinate singularity which appears at $(\xi_0,\eta_0)=(0.56,1.05)$ in this problem[16]. Furthermore, to resolve the flow information accurately at the sharp corner, a large number of mesh points are arranged in the vicinity of corner. Therefore, we consider the following mapping function of independent variables

$$x(\xi,\eta)=\lambda\xi+\frac{\mu}{\Gamma}(\xi\sinh2\xi-\eta\sin2\eta)\ ,$$

$$y(\xi,\eta)=\lambda\eta+\frac{\mu}{\Gamma}(\eta\sinh2\xi+\xi\sin2\eta) \tag{30}$$

herein, $\Gamma=\cosh(2\xi)+\cos(2\eta)$, and the constant λ, μ are defined as

$$\lambda=\frac{a+b}{4\tau},\quad \mu=\frac{a-b}{4\tau} \tag{31}$$

where a, b are the outlet, inlet heights of the constricting channel and are taken as $a=1$, $b=2$ respectively. In order to exclude the influence of the location of the inlet and outlet boundaries on the flow development, the inlet and outlet boundary are set at $x=-10$, $x=30$ far away from the constricted corner respectively. And then, as shown in Fig. 1(a), the corresponding boundary conditions for the above problem are listed as following:

$$u=1.5(1-y^2),\quad v=0,\quad \psi(y)=0.5y(3-y^2)$$

$$\text{as}\quad \xi\to-\infty \tag{32a}$$

$$v=u_\xi=\psi_\xi=0\quad \text{as}\quad \xi\to\infty \tag{32b}$$

$$u=v=0,\quad \psi=\tau\quad \text{on}\quad \eta=\tau \tag{32c}$$

$$u=v=0\quad \text{on}\quad \eta=-\tau \tag{32d}$$

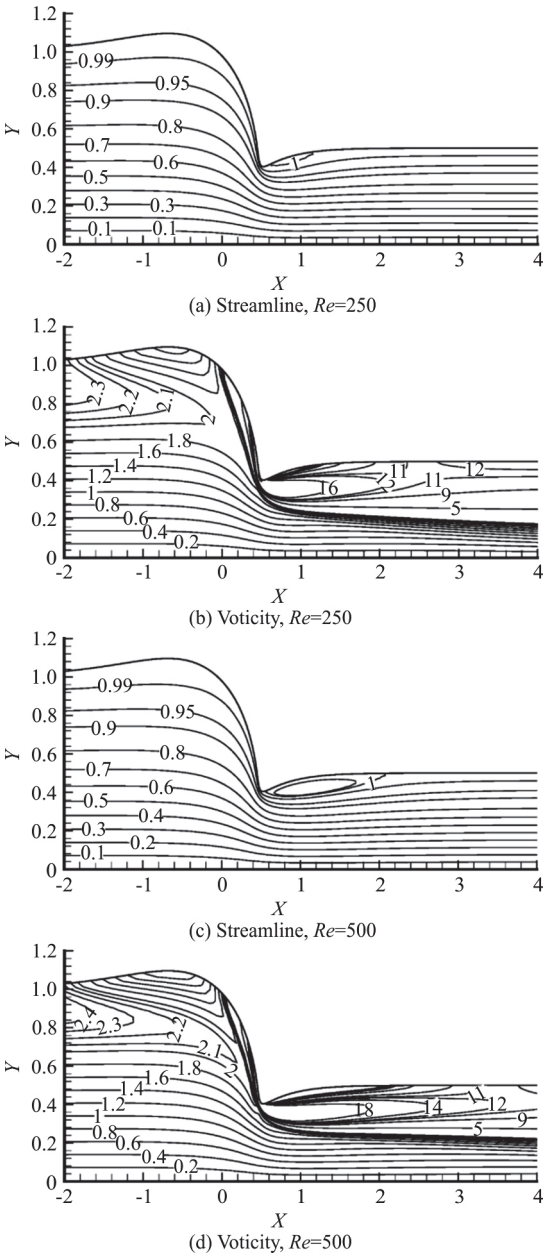

(a) Streamline, *Re*=250

(b) Voticity, *Re*=250

(c) Streamline, *Re*=500

(d) Voticity, *Re*=500

Fig. 2 Streamlines and vorticity contours for different Reynolds numbers with $\tau = 0.9$

It is worthy pointing out that, combining (30), (31), y will close to $(b\eta/2\tau)(a\eta/2\tau)$ when ξ appro- aches negative (positive) infinity. The qualitative results in terms of the streamlines and post processed vorticity contours for the constricted channel problem with $\tau = 0.9$, $Re = 250,\ 500$ are displayed in Fig. 2. The shape and value of the streamline and vorticity contour line are in good agreement with the results of Refs. [16, 18]. And the centreline velocity profiles for various Reynolds number and the controlling parameters are exhibited in Fig. 3. It is noticed that velocity profile is almost overlap for different Reynolds numbers and controlling parameters at the upstream of the throat. When the flow encounters the constriction in the vicinity of the throat, the centerline velocity profile occurs significant jump and the changed degrees increase with the controlling parameter $(0 < \tau \le 1)$ increases when fixed $Re = 500$. For $\tau = 0.8$, the changed degree of velocity profile is negative correlation with Re $(Re \le 1\,000)$, the main reason is that the width of the channel becomes more and more narrow with decreasing in Re or increasing in τ. In addition, the quantitative comparisons of the horizontal position of the separation and reattachment point on the upper wall vortex with various Reynolds numbers for $\tau = 0.9$ are tabulated in Table 2, it is clear that the current computational results are in good agreement with those results of Refs. [17-18].

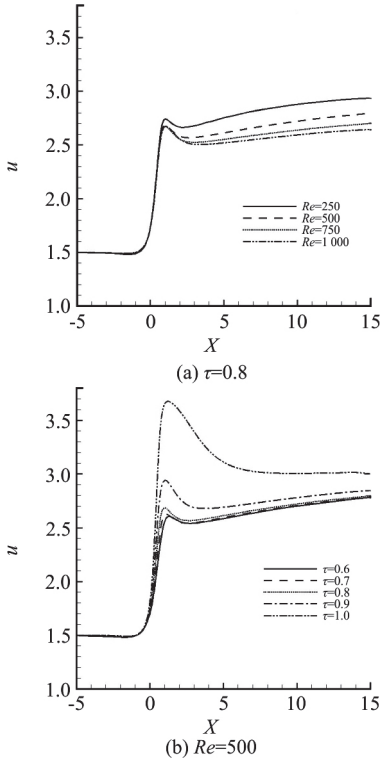

(a) τ=0.8

(b) *Re*=500

Fig. 3 Centerline velocity profile for the constricted channel problem

Table 2 Comparison of the separation and reattachment points on the upper wall vortex for $\tau = 0.9$

Re	Separation point			Reattachment point		
	Present	Ref. [17]	Ref. [18]	Present	Ref. [17]	Ref. [18]
175	0.69	0.68	0.66	0.88	0.86	0.85
200	0.64	0.62	0.61	1.10	1.00	1.10
250	0.60	0.59	0.57	1.20	1.20	1.30
500	0.55	0.53	0.52	2.10	2.10	2.30
600	0.54	0.51	0.51	2.50	2.40	2.80
750	0.54	0.51	0.51	3.10	3.00	3.50

3.3 *Driven polar cavity flow*

A fluid flow problem in a polar cavity, which was first researched by Fuchs and Tillmark[19] both experimental and numerical method, is nowadays being often employed to validate the capability of numerical algorithms for physical domains having circular arcs as boundaries. It is usually more difficult to capture accurately the flow character for some numerical algorithms than the square cavity flow problem because of its irregular geometrical shape. The schematic diagram of the polar cavity flow and boundary conditions are shown in Fig. 4, and the abbreviations V1, VL2 and VR2, VL3 refer to the primary vortex, left and right secondary vortex, tertiary vortex of the cavity flow, respectively. Meanwhile, we consider the following polar coordinate transformation

$$x(\xi,\eta)=\xi\cos\eta,\quad y(\xi,\eta)=\xi\sin\eta,$$

$$(\xi,\eta)\in[1,2]\times\left[\frac{\pi-1}{2},\frac{\pi+1}{2}\right] \tag{33}$$

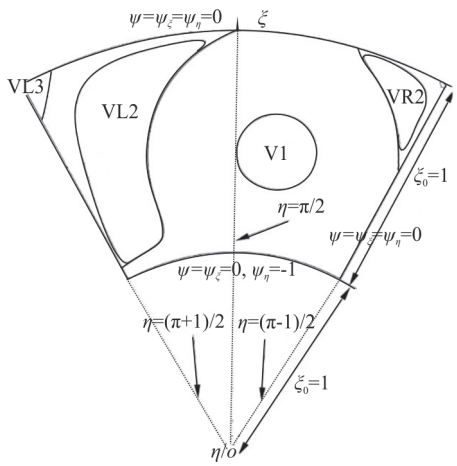

Fig. 4 Schematic diagram of the polar cavity flow and boundary conditions

In our calculation, the termination condition which the flow reaches steady states is that the absolute error tolerance $\left|\psi^{n+1}-\psi^{n}\right|\le 10^{-09}$ was achieved. Firstly, we present the comparisons of the steady-state streamfunction contour between our numerical and experimental results of Ref. [19] for $Re=55$, 350 in Fig. 5. Good agreement has been achieved between the current numerical and the experimental results. To illustrate the richness of the flow patterns, the computed streamlines and post processed vorticity contours for $0\le Re\le 3\,000$ are displayed in Fig. 6, it can be seen that two symmetrical secondary vortices about the radial line at $\eta=\pi/2$ are generated on the top left and right corner for $Re=0$. With increasing in Re, the two secondary vortices grow gradually in size, and the growth degree for the top left secondary vortex is larger than the top right one, at the same time, the primary vortex moves also towards the right side of the polar cavity center gradually. The small size tertiary vortex on the top left corner is captured for $Re\ge 2\,000$, As Reynolds number further increases, the small size tertiary vortex also gradually becomes larger, and the position of primary vortex almost becomes stabilization. The corresponding vorticity contours with $Re\le 3\,000$ are also shown in the right Fig. 6. All of the phenomena are accordant with those of Refs. [13, 20]. For $Re=5\,000$, the stable state results are given in Ref. [20] based on the steady N-S equations. However, We ran our code on the grids of size 81×81, 129×129 and 257×257 for computing the flow in $Re=5\,000$. Comparisons of the total energy, amplitude and frequency (f) for different grids with $Re=5000$ at dimensionless time $t=1\,000\text{-}1100$ are shown in Table 3. The total energy (E) and amplitude (A) are calculated by

$$E=\int_{\Omega}(u^2+v^2)\,\mathrm{d}\Omega,\quad A=\frac{E_{\max}-E_{\min}}{2} \tag{34}$$

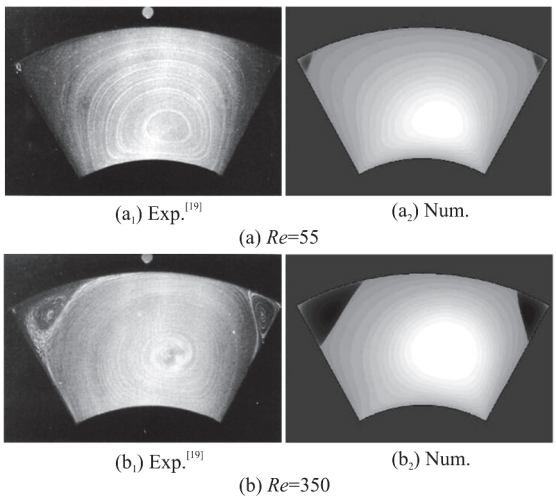

Fig. 5 Comparison of the steady-state streamlines

It is clear that the differences between 81×81, 129×129 and 257×257 grids about the average total energy, amplitude and frequency are no more than 1%. The partial time trace of total energy, Fourier frequency spectrum and phase-space trajectory at the monitoring point $(5/4,(2\pi+1)/4$ are displayed in Fig. 7 for $Re=5\,000$ with 129×129 grid. It indicates that the flow is not steady but time-periodic, which is

characterized by the fact that the frequency spectrum shows a spike ($f = 0.2224$) and its harmonics. We can also see from Fig. 7(c) that the phase trajectory of u versus v converges to a steady limit cycle, which manifests further that the flow is strictly periodic. In fact, the occurrence of a Hopf bifurcation is believed to take place at the Reynolds number lower than 3625 through our elaborate calculation. Finally the temporal evolution of streamlines for $Re = 5\,000$ on 129×129 grid are plotted during one period T_0 in Fig. 8.

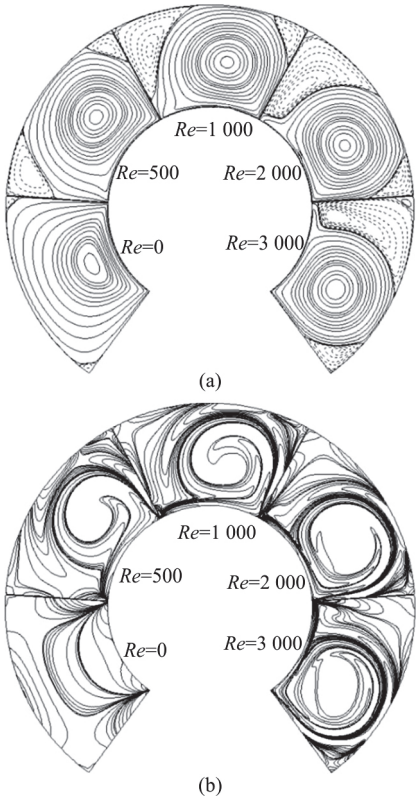

Fig. 6 The streamfunction (a) and vorticity (b) contours with 129×129 grid for different Reynolds numbers

Table 3 Comparison of the total energy, amplitude and frequency for different grid with $Re = 5\,000$

Grid	Average total energy	Amplitude	Frequency
81×81	6.29 (–02)	3.27 (–04)	0.22
129×129	6.35 (–02)	3.50 (–04)	0.22
257×257	6.44 (–02)	3.88 (–04)	0.23

Additionally, the quantitative data associated with the character of the primary, secondary and tertiary vortices for the driven polar cavity flow problem with $0 \le Re \le 3\,000$ are tabulated in Table 4. It can be noted that our results with other existing literature results[13, 20] are in excellent agreement when Reynolds number is less than 2 000. As for $Re = 3\,000$, there is a slight difference between the secondary and tertiary vortices.

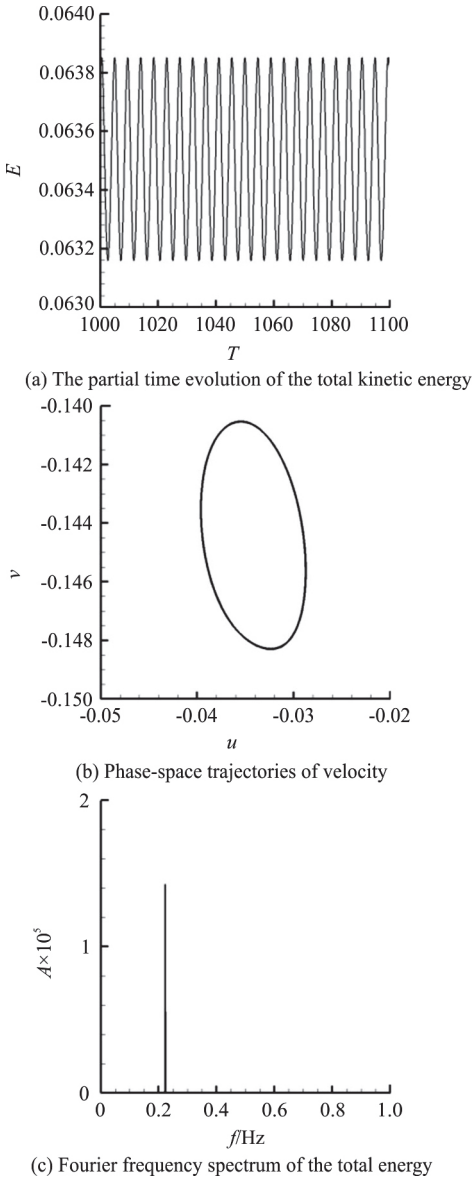

Fig. 7 Unsteady states at $Re = 5\,000$ with 129×129 grid

3.4 *Driven trapezoidal cavity flow*

In this section, to simulate fluid flow within isosceles trapezoidal cavity in Fig. 9, the following nonorthogonal transformation, which will map the trapezoidal domain in (x, y) plane to the rectangular domain in (ξ, η) plane, is introduced by

$$x(\xi,\eta) = F_1(y) + a[F_2(y) - F_1(y)]\xi\,,\quad y(\xi,\eta) = b\eta \tag{35}$$

where function $F_1(y) = -\tan\theta y$, $F_2(y) = 1 + \tan\theta y$ are relationships between x, y at two sides of the trapezoid, a, b are the stretching parameters. Both a, b are taken as 1 in our computation, and trape-

zoidal angle θ is set to $\pi/4$. The corresponding boundary conditions for the driven trapezoidal cavity flow problem are listed as following:

$$\psi = 0 \quad \text{on all four sides of } \Omega \tag{36a}$$

$$(\psi_x, \psi_y) \cdot \boldsymbol{t}_\omega = 1 \quad \text{on the top wall} \tag{36b}$$

$$(\psi_x, \psi_y) \cdot \boldsymbol{t}_\omega = 0 \quad \text{on the other three walls} \tag{36c}$$

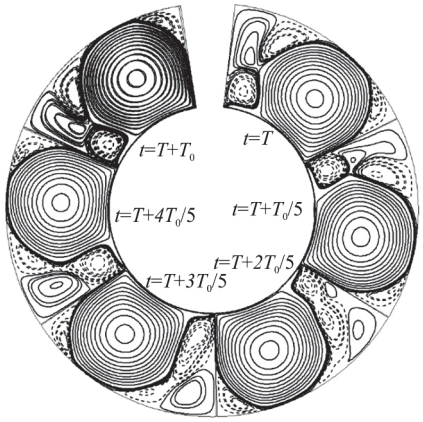

Fig. 8 The temporal evolution of streamlines on grid 129×129 for $Re = 5\,000$

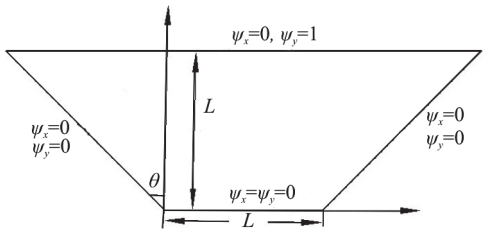

Fig. 9 Schematic diagram of the trapezoidal cavity flow and boundary conditions

where Ω represents the boundary area, and $\boldsymbol{t}_\omega$ is a unit vector tangent of boundary in the direction of motion.

In Table 5, the minimum values of streamfunction $(\psi_{\min})$ the central locations (x_0, y_0) of the primary vortex and post processed vorticity (ω_0) at these locations are compared with the results of Mcquain et al.[21] and Zhang et al.[22] As seen from Table 5, the present computational results are in good agreement with those results of Refs. [21-22]. Meanwhile, streamline patterns for the trapezoid with Re = 100, 500 are shown in Fig. 10, it is clear that the shapes of the streamline agree excellently with the available results of Ref. [21]. Figure 11 shows the computed streamlines patterns for $100 \le Re \le 1\,000$. For $Re = 1\,00$, the central eddy is seen to occupy the whole region of the trapezoidal cavity. As the Reynolds number is increased to 400, the two secondary circulations occur at the bottom corner regions and the left secondary eddy is greater than the right one in size. With increase in Reynolds number, the two secondary eddies coalesce into one. As Re is increased further, the secondary eddy gains a more significant size, it can be seen from Fig. 11(d) that the primary vortex is compressed and splits into two individual vortices.

4. Conclusions

In the present paper, a temporal and spatial second-order accurate compact difference scheme for solving the time-dependent incompressible N-S equations based on streamfunction-velocity (pure streamfunction) formulation is proposed in the arbitrary curvilinear coordinates. The main advantages of the current algorithm are that it is established based on the arbitrary curvilinear coordinates and the coefficient

Table 4 The results of primary, secondary and tertiary vortices with different Reynolds numbers

Re	Sources	Primary	Location	VL2	VR2	VL3	VR3
0	Yu[13]	0.11366	(0,1.281)	–4.74 (–06)	–4.74 (–06)	-	-
	Present	0.11365	(0,1.273)	–4.70 (–06)	–4.70 (–06)	-	-
55	Yu[13]	0.11554	(0.141,1.281)	–4.69 (–06)	–8.69 (–06)	-	-
	Sen[20]	0.11550	(0.138,1.285)	–4.99 (–06)	–7.96 (–06)	-	-
	Present	0.11554	(0.141,1.281)	–4.69 (–06)	–8.67 (–06)	-	-
350	Yu[13]	0.12633	(0.167,1.416)	–3.99 (–04)	–5.49 (–04)	-	-
	Sen[20]	0.12630	(0.163,1.411)	–4.01 (–04)	–5.47 (–04)	-	-
	Present	0.12632	(0.166,1.412)	–3.94 (–04)	–5.48 (–04)	-	-
500	Sen[20]	0.12730	(0.165,1.423)	–1.19 (–03)	–1.01 (–03)	-	-
	Present	0.12708	(0.167,1.429)	–1.17 (–03)	–1.01 (–03)	-	-
1 000	Yu[13]	0.12753	(0.169,1.439)	–3.46 (–03)	–2.12 (–03)	-	-
	Sen[20]	0.12750	(0.166,1.436)	–3.48 (–03)	–2.10 (–03)	-	-
	Present	0.12749	(0.169,1.435)	–3.38 (–03)	–2.10 (–03)	-	-
2 000	Yu[13]	0.12529	(0.188,1.449)	–4.83 (–03)	–3.00 (–03)	-	-
	Present	0.12538	(0.182,1.450)	–4.75 (–03)	–2.95 (–03)	4.72 (–07)	-
3 000	Sen[20]	0.12400	(0.196,1.447)	–7.09 (–03)	–3.32 (–03)	3.64 (–06)	-
	Present	0.12422	(0.193,1.448)	–4.33 (–03)	–3.30 (–03)	2.87 (–06)	-

Table 5 Validation of present simulations for trapezoidal cavity with $Re = 100,500$

Re	Sources	$\psi_{\min}$	ω_0	Location (x_0, y_0)
100	McQuain et al.[21]	0.2900	1.1050	(2.023, 2.193)
	Zhang et al.[22]	0.2868	1.0960	(2.0273, 2.1914)
	Present results	0.2904	1.1009	(2.0216, 2.2031)
500	McQuain et al.[21]	0.3170	0.9640	(1.848, 2.055)
	Zhang et al.[22]	0.3135	0.9493	(1.8457, 2.0508)
	Present results	0.3185	0.9675	(1.8392, 2.0625)

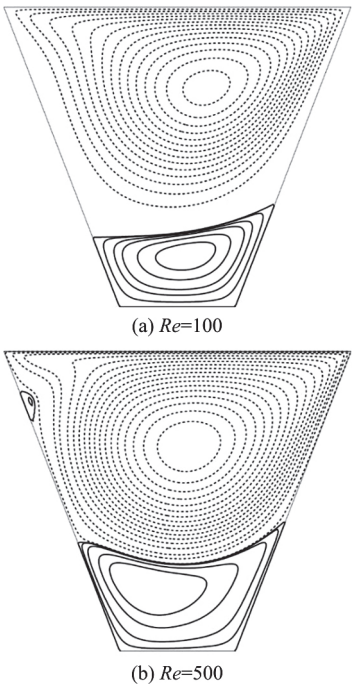

Fig. 10 Streamline patterns for the trapezoid

matrix based on five-point compact stencil is constant and satisfies strictly penta-diagonal dominant which can ensure stability for the discrete algebraic system utilizing conventional iterative method. Compared with the established numerical and experimental results, our present algorithm has been verified that it is quite effective and the numerical results agree excellently with the available results in literatures.

We apply current approach to four problems which encompass an analytical solution for the boundary layer, constricted channel problem, driven polar cavity flow and trapezoidal cavity flow problem. The robustness and effectiveness of the scheme are demonstrated in the above cases. The relevant tabular data imply that the present compact scheme achieves the theoretical convergence accuracy as expected and is slightly better than numerical results for other available second order schemes. For the driven polar cavity flow problem, the relevant data and graphs show that our current computed solutions are in excellent agreement with the existing numerical results for $0 \le Re \le 3\,000$. For $Re = 5\,000$, as displayed in Fig. 7, the frequency spectrum shows a spike $(f = 0.2224)$ and its harmonics, the phase trajectories of u versus v converge to a steady limit cycle. The facts show that the corresponding flow with $Re = 5\,000$ is not steady but-time-periodic flow with a period close to 4.5. Meanwhile, the occurrence of a Hopf bifurcation is believed to take place at the Reynolds number lower than 3 625 through our elaborate calculation. For the driven trapezoidal cavity flow case, which is the nonorthogonal transformation problem, our computational results are in excellent agreement with the established numerical results.

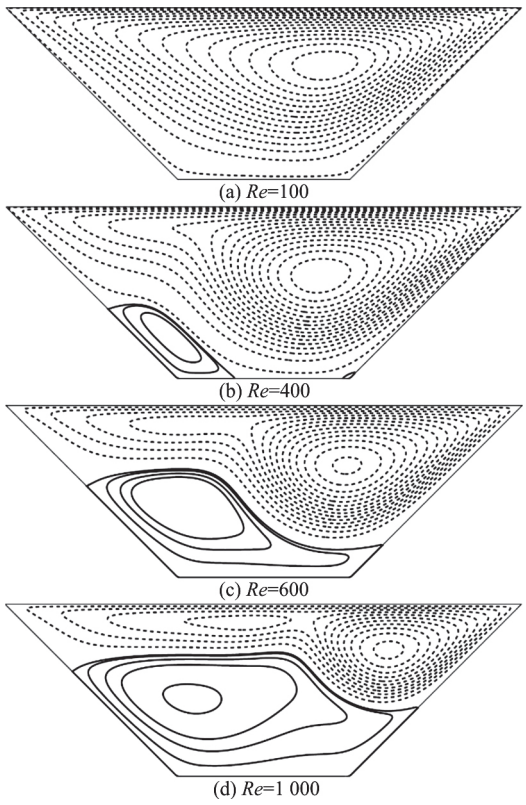

Fig. 11 Streamline and vorticity contours for the trapezoid with various Reynolds numbers

Acknowledgement

This work was supported by the China Postdoctoral Science Foundation (Grant No. 2014M550211).

References

[1] Tian Z. F., Ge Y. B. A fourth-order compact finite difference scheme for the steady stream function-vorticity formulation of the Navier-Stokes/Boussinesq equations [J]. *International Journal for Numerical Methods in Fluids,* 2003, 41(5): 495-518.

[2] Wang J., Zhong W., Zhang J. High order compact com-

putation and nonuniform grids for streamfunction vorticity equations [J]. *Applied Mathematics and Computation*, 2006, 179(1): 108-120.

[3] Ge Y., Cao F. Multigrid method based on the transformation-free HOC scheme on nonuniform grids for 2D convection diffusion problems [J]. *Journal of Computational Physics*, 2011, 230(10): 4051-4070.

[4] Bonaventura L., Ferretti R., Rocchi L. A fully semi-Lagrangian discretization for the 2D incompressible Navier–Stokes equations in the vorticity-streamfunction formulation [J]. *Applied Mathematics and Computation*, 2018, 323:132-144.

[5] Yu P. X., Xiao Z., Wu S. et al. High accuracy numerical investigation of double-diffusive convection in a rectangular cavity under a uniform horizontal magnetic field and heat source [J]. *International Journal of Heat and Mass Transfer,* 2017, 110: 613-628.

[6] Fishelov D., Ben-Artzi M., Croisille J. P. Recent developments in the pure streamfunction formulation of the Navier-Stokes system [J]. *Journal of Scientific Computing,* 2010, 45(1-3): 238-258.

[7] Tian Z. F., Yu P. X. An efficient compact difference scheme for solving the streamfunction formulation of the incompressible Navier-Stokes equations [J]. *Journal of Computational Physics*, 2011, 230(17): 6404-6419.

[8] Kalita J. C., Gupta M. M. A streamfunction-velocity approach for the 2D transient incompressible viscous flows [J]. *International Journal for Numerical Methods in Fluids*, 2010, 62(3): 237-266.

[9] Pandit S. K., Karmakar H. An efficient implicit compact streamfunction velocity formulation of two dimensional flows [J]. *Journal of Scientific Computing*, 2016, 68(2): 653-688.

[10] Yu P. X., Tian Z. F. An upwind compact difference scheme for solving the streamfunction-velocity formulation of the unsteady incompressible Navier-Stokes equation [J]. *Computers and Mathematics with Application*, 2018, 75(9): 3224-3243.

[11] Kupferman P. A central difference scheme for a pure streamfunction formulation of incompressible viscous flow [J]. *SIAM Journal on Scientific Computing*, 2001, 23(1): 1-18.

[12] Pérez Guerrero J. N. N., Quaresma J. N. N., Cotta R. M. Simulation of laminar flow inside ducts of irregular geometry using integral transforms [J]. *Computational Mechanics*, 2000, 24(4): 413-420.

[13] Yu P. X., Tian Z. F. A compact scheme for the streamfunction-velocity formulation of the 2D steady incompressible Navier-Stokes equations in polar coordinates [J]. *Journal of Scientific Computing*, 2013, 56(1): 165-189.

[14] Pandit S. K. On the use of compact streamfunction-velocity formulation of steady Navier-Stokes equations on geometries beyond rectangular [J]. *Journal of Scientific Computing*, 2008, 36(2): 219-242.

[15] Sen S., Kalita J. C., Gupta M. M. A robust implicit compact scheme for two-dimensional unsteady flows with a biharmonic stream function formulation [J]. *Computer and Fluids*, 2013, 84: 141-163.

[16] Mancera P. F. A. A study of numerical solution of the steady two dimensional Navier-Stokes equations in a constricted channel problem by a compact fourth order method [J]. *Applied Mathematics and Computation*, 2003, 146(2-3): 771-790.

[17] Abdullah S., Guo H., Yuan L. A third-order upwind compact scheme on curvilinear meshes for the incompressible Navier-Stokes equations [J]. *Communications in Computational Physics*, 2009, 5(2-4): 712-729.

[18] Pandit S. K., Kalita J. C., Dalal D. C. A fourth-order accurate compact scheme for the solution of steady Navier-Stokes equations on non-uniform grids [J]. *Computer and Fluids*, 2008, 37(2): 121-134.

[19] Fuchs L., Tillmark N. Numerical and experimental study of driven flow in a polar cavity [J]. *International Journal for Numerical Methods in Fluids*, 1985, 5(4): 311-329.

[20] Sen S., Kalita J. C. A 4OEC scheme for the biharmonic steady Navier-Stokes equations in non-rectangular domains [J]. *Computer Physics Communications*, 2015, 196: 113-133.

[21] McQuain W. D., Ribbens C., Wang C. W. Steady viscous flow in a trapezoidal cavity [J]. *Computer and Fluids*,1994, 23(4): 613-626.

[22] Zhang T., Shi B., Chai Z. Lattice Boltzmann simulation of lid-driven flow in trapezoidal cavities [J]. *Computer and Fluids*, 2010, 39(10): 1977-1989.